ORIGINAL PAPER

Blended gold/MnO2@BSA nanoparticles for fluorometric and magnetic resonance determination of ascorbic acid

Jiani Yu [1,2] · Weitao Yang [1] · Shige Xing [3] · Jun Wang [1] · Huanxing Han [4] · Pengfei Zhang [4] · Chenyang Xiang [1] · Bingbo Zhang [1]

Abstract

A fluorometric and magnetic resonance (MR) dual-modal detection scheme is presented for determination of ascorbic acid (AA). It is based on the use of a blended Au/MnO2@BSA mixture that was prepared via a biomimetic strategy, using bovine serum albumin (BSA) as the template at physiological temperature. The MnO2@BSA fraction (one part of the composite) is not susceptible to MR but can be degraded to MR-active compounds upon a redox reaction with even ultralow concentrations of AA. In parallel, the blended Au/MnO2@BSA recovers its fluorescence because MnO2@BSA acts as a quencher of the fluorescence of circumjacent Au@BSA (the other part of the composite). Fluorescence typically is measured at excitation/emission wavelengths of 470/625 nm. Leveraging on this redox reaction between MnO2 and AA, a dual-mode detection scheme for AA was developed. Both the fluorescence and the MR signal increase with the concentration of AA. The lowest limit for the detection of AA is 0.6 μM in the fluorometric mode and 0.4 μM in the MR mode. Analysis of AA-spiked serum samples showed that the recoveries obtained by either the fluorometric and MR mode can reach 94%. This is the first report of the use of blended nanoparticles with their inherent cross-validation regularity.

Keywords Biomimetic approach · Ascorbic acid · Dual-modal detection

Introduction

Ascorbic acid (AA, also known as vitamin C) plays important roles in many metabolic processes [1–3]. It is vital to develop

---

Jiani Yu, Weitao Yang and Shige Xing contributed equally to this work.

✉ Bingbo Zhang
bingbozhang@tongji.edu.cn

1   Institute of Photomedicine, Shanghai Skin Disease Hospital, The Institute for Biomedical Engineering & Nano Science, Tongji University School of Medicine, Shanghai 200443, People's Republic of China

2   Chongqing University of Education, Chongqing 400067, People's Republic of China

3   Institute of Food Safety, Chinese Academy of Inspection & Quarantine, Beijing 100176, People's Republic of China

4   Department of Pharmacy, Changzheng Hospital, Second Military Medical University, Shanghai 200003, People's Republic of China

detection methods of AA in pharmaceutical preparations, food products, and clinical diagnosis. Various analytical approaches have been developed for detecting AA, such as fluorometry [4], chemiluminescence [5], and electrochemical method [6–8], of which fluorometry has attracted more attention because of their outstanding sensitivity and rapid implementation [9]. Fluorescent detecting probes for AA were formed with different sensors, such as quantum dots [10], up-conversion materials [11], rare earth persistent luminescence nanoparticles [12], and Au nanoclusters [13]. Although fluorescent methods own numerous virtues, any single detection mode has its inherent limitations. Thus, it is remarkable to improve the detection performance of fluorescent methods by combining with other complementary measuring strategies. MR-based assay is homogeneous, light-independent, and easy to operate compared to colorimetric assay and fluorometry [14]. Consequently, fluorescence/MR dual-modal strategy is considered to be a promising approach to acquire more accurate clinical diagnosis information [15, 16]. For instance, Xu et al. developed a magnetic/fluorometric bimodal sensor for GSH based on CDs-MnO2 platform [16]. Chen et al. compounded Eu(DPA)3/Gd(DPA)3@Lap as MR/

fluorescence dual-modal sensor for AA detection [15]. Nevertheless, these functional materials were synthesized by complicated chemical steps, which hamper their future biomedical applications due to their environmentally unfriendly characteristics and poor reproduction. It also should be pointed out that few interactions existed in the reported sensing materials in the dual-modal detection. Thus, the development of measuring strategies using cross-validation of dual-modal detection based on eco-friendly materials is of great importance.

Inspired by bio-mineralization, a green process that employs peptides or proteins as bio-templates to synthesize inorganic nanoparticles has been observed. Compared with traditional chemical strategies, this strategy presents multiplicity of advantages, including milder synthesis conditions, no organic solvents, good bio-compatibility and reproduction [17, 18]. Bovine serum albumin (BSA) has been demonstrated a good template to prepare inorganic nanoparticles for biomedical applications [19, 20]. By using this bio-mimetic strategy, our group has successfully prepared a series of function nanoparticles for bio-imaging applications, such as the positive blood pool contrast agent with high relaxivity and a prolonged imaging time window [21], tiny tumor bimodal targeted imaging in vivo [22], and photoacoustic/MR imaging-guided tumor-targeted photothermal therapy [23]. The above nanoparticles were formed in a single particle state, even for those multi-functional nanoparticles.

Hence, we describe a BSA-mediated strategy for biomimetic synthesis of blended Au@BSA and MnO$_2$@BSA mixture nanoparticles, denoted Au/MnO$_2$@BSA, in a one–pot manner for fluorometric/MR dual-modal cross-validation detection of AA in human serum. As outlined in Scheme 1, in the absence of AA, the red luminescence at 625 nm wavelength of Au@BSA can be efficiently quenched by the circumjacent MnO$_2$@BSA. However, in the presence of AA, the red luminescence of Au@BSA recovers due to the degradation of MnO$_2$@BSA by AA, and particularly, MR is activated along with the degradation of the original MR-inert MnO$_2$@BSA into MR-active compounds. Based on measuring the changes of fluorescence and MR signals, the involved AA concentration can be calculated in a cross-validation dual-modal detection fashion.
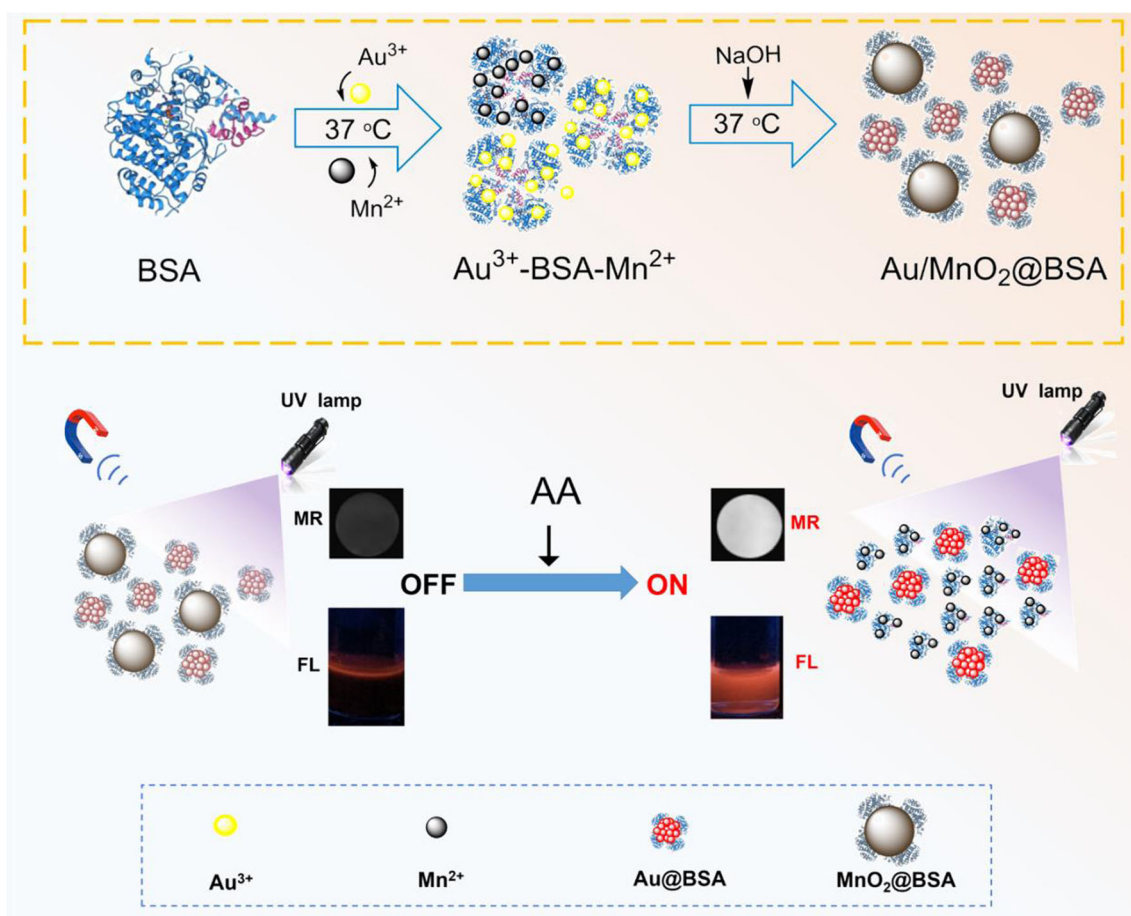
Scheme 1 Schematic of biomimetic synthesis of blended Au/MnO$_2$@BSA and the process of detecting AA

Experimental section

Materials

Manganese chloride tetrahydrate ($MnCl_2 \cdot 4H_2O$), sodium hydroxide, and N-Ethylmaleimide were purchased from Aladdin Reagent Co., Ltd. (Shanghai, China, www.aladdin-e.bioon.com.cn). Bovine serum albumin (BSA) was purchased from Alfa Aesar China Co., Ltd. (www.alfachina.cn). $HAuCl_4 \cdot 4H_2O$ was bought from HWRK Chem Co., Ltd. (Beijing, China, www.hwrkchemical.com). L-ascorbic acid, Tris-acetate-EDTA, and other salts were purchased from Sinopharm Chemical Reagent Co., Ltd. (Shanghai, China, www.reagent.com.cn). Agarose gel was purchased from Yeasen Biotech Co. Ltd. (Shanghai, China, www.yeasen.com). All chemicals were used without further purification. Deionized water (18.2 MΩ·cm resistivity at 25 °C) was used throughout the entire experiments.

One-pot biomimetic synthesis of blended Au/MnO$_2$@BSA nanoparticles

Briefly, 125 mg of BSA was dissolved in 50 mL of ultrapure water, then 0.25 mL of 100 mM $MnCl_2 \cdot 4H_2O$ and 1 mL of $HAuCl_4 \cdot 4H_2O$ (25 mM) were added into above solution slowly under stirring at 37 °C. Three minutes later, 0.5 mL of NaOH (1 M) was injected into the reaction flask, maintained at 37 °C for 12 h. Finally, the product was dialyzed against deionized water for 24 h to remove excess precursors.

Biomimetic synthesis of individual Au@BSA and MnO$_2$@BSA nanoparticles

Au@BSA nanocluster was synthesized following the reported method [24]. The synthetic method of MnO$_2$@BSA nanoparticle is similar to that of the blended Au/MnO$_2$@BSA. The experimental procedures are provided in the supporting information.

Material characterizations

The size and morphology of nanoparticles were obtained by transmission electron microscopy (TEM, G2 F20, Tecnai). The photoluminescence spectra and UV − visible absorption spectra were measured using LS-55 fluorescence spectrometer (PerkinElmer) and Cary 50 UV-vis spectrophotometer (Varian), respectively. Hydrodynamic diameter and size distribution of nanoparticles were measured by a dynamic light scattering (DLS) analyzer (nano-ZS, Malvern). The relaxation times were measured on a 1.5 T minispec mq 60 NMR analyzer (Bruker, Germany). The X-ray photoelectron spectroscopy (XPS) measurements were performed using a PHI-5000

CESCA system (PerkinElmer) with radiation from an Al Kα (1486.6 eV) X-ray source.

Colloidal stability studies

The nanoparticles ware dispersed in ultrapure water and phosphate buffered saline (pH 7.4), respectively. Stability studies were evaluated by monitoring the changes of size distribution, UV-vis absorption, fluorescence intensity and longitudinal relaxation time (T_1).

Gel electrophoresis analysis

Briefly, 5 μL of the solution of Au@BSA, MnO$_2$@BSA, the blended Au/MnO$_2$@BSA and Au@BSA + MnO$_2$@BSA were loaded onto a 2% agarose gel respectively. Subsequently, the electrophoresis experiments were carried out in 1 × Tris-acetate-EDTA (TAE) at 80 V for 60 min. Finally, the imaging of the gel was obtained by a digital camera.

The sensitivity study of blended Au/MnO$_2$@BSA for AA detection

1 mL of the blended Au/MnO$_2$@BSA aqueous solution (2 mg/mL) was added to a centrifuge tube, and then 1 mL of AA solution with different concentrations (0, 4, 8, 20, 40, 80, 100, 200, 400 and 600 μM) was slowly titrated. The changes of fluorescence spectra and relaxation times of the mixture were recorded after reaction, respectively.

The selectivity study of blended Au/MnO$_2$@BSA for AA detection

To evaluate the selectivity of blended Au/MnO$_2$@BSA for AA detection, the responses of blended Au/MnO$_2$@BSA were investigated by adding various interfering substances including L-glutamine (L-Gln), Glucose (Glc), L-alpha-Alanine, L-Alanine, L-Histidine (L-His), Cysteine (Cys), Glutathione (GSH), Cu^{2+}, Na^+, Ca^{2+}, K^+, Mg^{2+}, and Fe^{3+} to 1 mL of blended Au/MnO$_2$@BSA solution (2 mg/mL), respectively. The changes of fluorescence spectra and relaxation times of the mixture were recorded, respectively. The concentrations of Cu^{2+}, L-Gln, Glc, L-alpha-Alanine, L-Alanine, L-His, Cys, and GSH were 0.1 mM, while Na^+, Ca^{2+}, K^+, Mg^{2+}, Fe^{3+} were 1 mM.

Detection of AA in human serum

To evaluate the detection efficiency of Au/MnO$_2$@BSA in actual samples, serum samples collected with heparin anticoagulant technology were diluted 15-fold and added NEM (1.35 μM). Then, serum sample (1 mL) was mixed with 1 mL of Au/MnO$_2$@BSA aqueous solution (2 mg/mL) to obtain the original content of AA under fluorescence and

MR mode. Finally, the serum samples were added into different concentrations of AA (5, 10, and 15 μM), followed by be measured again to calculate sample recovery rate.

Results and discussion

Preparation and characterizations of blended Au/MnO$_2$@BSA

Blended Au/MnO$_2$@BSA mixture nanoparticles were synthesized by a one-pot biomimetic mineralization approach. The detailed reaction mechanism is discussed in literatures [25, 26]. In order to reveal the formation process of the blended Au/MnO$_2$@BSA, we monitored the change of UV–vis absorption and fluorescence spectra of at different time points (2 min, 5 min, 10 min, 1 h, 2 h, 6 h, and 12 h). The UV–vis absorption spectra shown in Fig. S1 in the electronic supporting information show a comparison with the absorbance spectrum of BSA. The formation of a new absorption band between 300 and 450 nm is observed after 5 min. The steady increase while the reaction continues is attributed to the surface plasmon absorbance of MnO$_2$ [27]. Then, their corresponding fluorescence spectra were also recorded (Fig. S2, supporting information). After 6 h, it was found an emission peak at 625 nm detected under excitation at 470 nm, and this emission goes up along with the reaction time.

By lyophilized, the obtained light brown flocculent powder can be easily redissolved in ultrapure water (Fig. 1a inset). The corresponding transmission electron microscope (TEM) image displays Au@BSA and MnO$_2$@BSA are blended in the field (Fig. 1a). Further TEM characterizations show Au@BSA and MnO$_2$@BSA nanoparticles have different sizes, namely, 1–2 nm of Au@BSA and 20–25 nm of MnO$_2$@BSA (Fig. S3A and S3B). Based on the measurement of interplanar distances, we can confirm that the co-existence of Au@BSA and MnO$_2$@BSA nanoparticles. The blended state of nanoparticles was also verified by a DLS analyzer. It
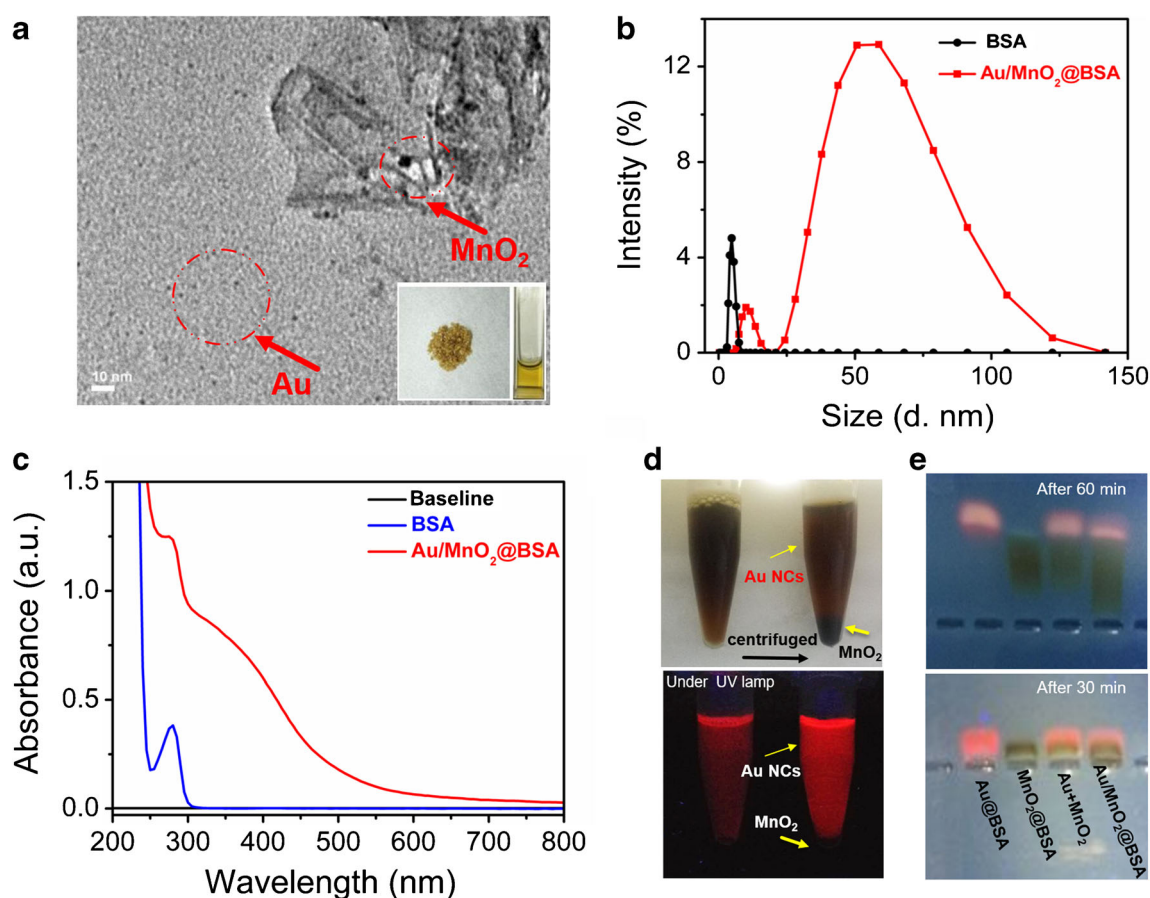

Fig. 1 Characterizations of the blended Au/MnO$_2$@BSA. **a** TEM image of blended Au/MnO$_2$@BSA. Inset: Digital photographs of lyophilized powder of Au/MnO$_2$@BSA and its redissolved solution in water. **b** Size and distribution of BSA and the blended Au/MnO$_2$@BSA. **c** UV-vis absorption spectrum of BSA and the blended Au/MnO$_2$@BSA. **d** The digital photographs of the blended Au/MnO$_2$@BSA solution before and after centrifugation (the upside: under an incandescent lamp, the bottom: under a UV lamp). **e** Gel electrophoresis after 30 min and 60 min of running time were photographed under a UV lamp excitation (from left to right: Au@BSA, MnO$_2$@BSA, Au + MnO$_2$ and the blended Au/MnO$_2$@BSA)

shows a double-peak pattern, which appoints to Au@BSA (the smaller size) and MnO_2@BSA (the larger size) (Fig. 1b). The UV-vis absorption spectrum of the blended Au/MnO_2@BSA is shown in Fig. 1c. It has at least two characteristic peaks, which belong to the BSA (around 280 nm) and MnO_2 (around 300 nm–450 nm), respectively. The valence states of Au and Mn elements in the blended nanoparticles were investigated by XPS. Fig. S4A shows the survey of XPS spectrum of the blended Au/MnO_2@BSA, and clearly presents the co-existence of Au and Mn elements in the sample. Fig. S4B shows that the core-level XPS spectrum of Au 4f7/2 consists of two components at 84.0 eV and 85.0 eV (red and pink). These can be assigned to Au(0) and Au(I) respectively [24, 28]. The binding energies of Mn centered at 653.8 eV and 642.4 eV (Fig. S4C), corresponding to Mn(IV) 2p 1/2 and Mn (IV) 2p 3/2 spin–orbit peaks of MnO_2 [29].

In order to intuitively disclose the blended state of Au/MnO_2@BSA, we first used centrifugation to separate the Au@BSA from MnO_2@BSA by leveraging on the difference in their density. As shown in the Fig. 1d, the original uniform blended solution in appearance is clearly divided into two parts after centrifugation at 13800 rpm for 30 min. The upper supernatant is the solution of Au@BSA, while the under sediment layer is the solution of MnO_2@BSA. Under a UV lamp excitation, we can distinctly observe bright fluorescent emission of the upper layer and none-emission of the down layer. Interestingly, compared with the unseparated solution, the supernatant solution after centrifugation has much stronger fluorescence signal. Based on this evidence, we believe that Au@BSA and MnO_2@BSA individually exist in the original solution. Because of the quenching effect of MnO_2@BSA, fluorescent Au@BSA in the original solution has weak fluorescence, but after separation from each other, its fluorescence recovers. To be doubly sure, gel electrophoresis was used to further prove the mixed state of Au/MnO_2@BSA in another side. Gel electrophoresis technique has been reported to be used to sort nanoparticles [30–32]. As shown in the Fig. 1e, blended Au/MnO_2@BSA run in 2% agarose gel in 1 × TAE (Tris-borate EDTA) buffer together with the mixed solution of Au@BSA and MnO_2@BSA (Au + MnO_2), MnO_2@BSA solution and Au@BSA solution. The result shows a clear separation of Au@BSA (red) from the MnO_2@BSA (brown) in the blend Au/MnO_2@BSA lane.

Stability analysis

The stability assessment of the blended Au/MnO_2@BSA was investigated through incubation with DI water and phosphate-buffered saline (PBS) over 7 days. As presented in Fig. S5A and S5B, the hydrodynamic diameter of the blended Au/MnO_2@BSA is stable. The UV−vis absorption spectra of the blended Au/MnO_2@BSA also remain almost unchanged, which is shown in the Fig. S5C and S5D. Taken together,

these results suggest the good colloidal stability of the blended nanoparticles for at least 7 days. As displayed in Fig. S5E, the fluorescence intensity at 625 nm of the blended Au/MnO_2@BSA remained almost unchanged, and the corresponding fluorescent emission spectra was shown in the Fig. S6. Moreover, no significant change is observed in longitudinal relaxation times (T_1) (Fig. S5F). So, we think this good stability of the blended Au/MnO_2@BSA is beneficial to their biomedical applications.

Response capability study for AA

The component of MnO_2@BSA in the blended solution can react with AA, resulting in the degradation of MnO_2@BSA nanoparticles into Mn^{2+}. This format transform can be reflected on the changes of size, UV-vis absorption spectrum, fluorescent emission and relaxation rate. Thus, we used these four physical signals to assess the response capability of the blended Au/MnO_2@BSA for AA.

After addition of AA, the size of the blended Au/MnO_2@BSA is reduced to the size of Au@BSA, as shown in Fig. 2a, suggesting an efficient degradation of MnO_2@BSA by AA. Moreover, the appearance color turns to be almost transparent after addition of AA, as shown in the inset of Fig. 2a. UV-vis absorption spectra further reveal the collapse of MnO_2@BSA in the blended solution by AA, in which the characteristic absorption band at 300 nm–450 nm of the MnO_2@BSA disappears after addition of AA, while the absorption band at 280 nm has no noticeable change (Fig. 2b). It can be therefore concluded that in the presence of AA, MnO_2@BSA is reduced to Mn^{2+}, leading to small size and vanishing of the absorption peak of MnO_2. Concurrently, the fluorescent emission is significantly recovered as shown in Fig. 2c. This emission enhancement is attributed to the degradation of MnO_2@BSA, resulting in the disappearance of the quenching effect on Au@BSA. Particularly, the longitudinal relaxation rate (r_1) is improved to 11.245 $mM^{-1} \cdot s^{-1}$ in the presence of AA from that of original blended solution (r_1 = 2.4749 $mM^{-1} \cdot s^{-1}$), as shown in Fig. 2d. The MR enhancement is due to the degradation of MR-inert MnO_2@BSA into MR-active Mn^{2+} and its further binding with macromolecular BSA [31]. The corresponding T_1-weighted MR images (Fig. 2e) and their relative quantified signal intensities (Fig. S7 in supporting information) are provided.

Optimizing the detecting conditions

In order to measure the precise AA concentration, the concentration of the Au/MnO_2@BSA and detection time were optimized. 1 mL of the blended Au/MnO_2@BSA with different concentrations (0.5, 1, 2, 4, and 8 mg/mL) were used to detect AA (100 μM), respectively. This concentration of AA is chosen for testing because it is reported that the concentrations of AA in
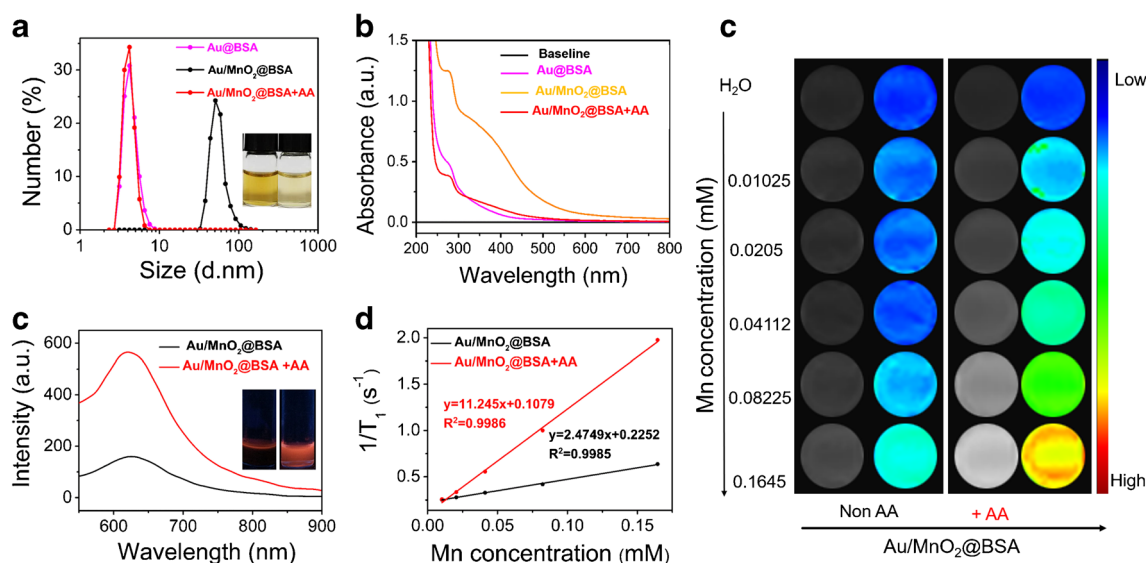
Fig. 2 The response capability of the blended Au/MnO$_2$@BSA for AA. The changes of size (**a**), UV-vis absorption spectrum (**b**), fluorescent emission (**c**), and relaxation rate (**d**). **e** The T$_1$-weighted MR images and pseudo-color-map of the blended Au/MnO$_2$@BSA at varying Mn concentrations ranging from 0 to 0.1645 mM (the left: in the absence of AA, the right: in the presence of AA)

the human serum range from 20 μM to 100 μM [14]. As presented in Fig. S8A and S8B, the fluorescence intensities at 625 nm and longitudinal relaxation time (T$_1$) of Au/MnO$_2$@BSA gradually increased in the range of 0 to 2 mg/mL, and then show a downtrend. This result indicated that the optimized Au/MnO$_2$@BSA concentration was 2 mg/mL under fluorometric or MR mode. Then, 1 mL of the blended Au/MnO$_2$@BSA (2 mg/mL) were used to detect AA (100 μM) to optimize the detection time from 10 min to 12 h. As shown in the Fig. S8C and S8D, 8 h is need for the completion of the reaction.

Admittedly, we should figure out how to shorten the detection time, that is what we will focus on in the near future work.

Sensitivity and selectivity study

Under the optimized experimental conditions, the sensitivity was investigated by incubating the blended Au/MnO$_2$@BSA with different concentrations of AA. As shown in Fig. 3a, the color of the reaction solution gradually fades and a gradient fluorescence recovery is observed along with the increased
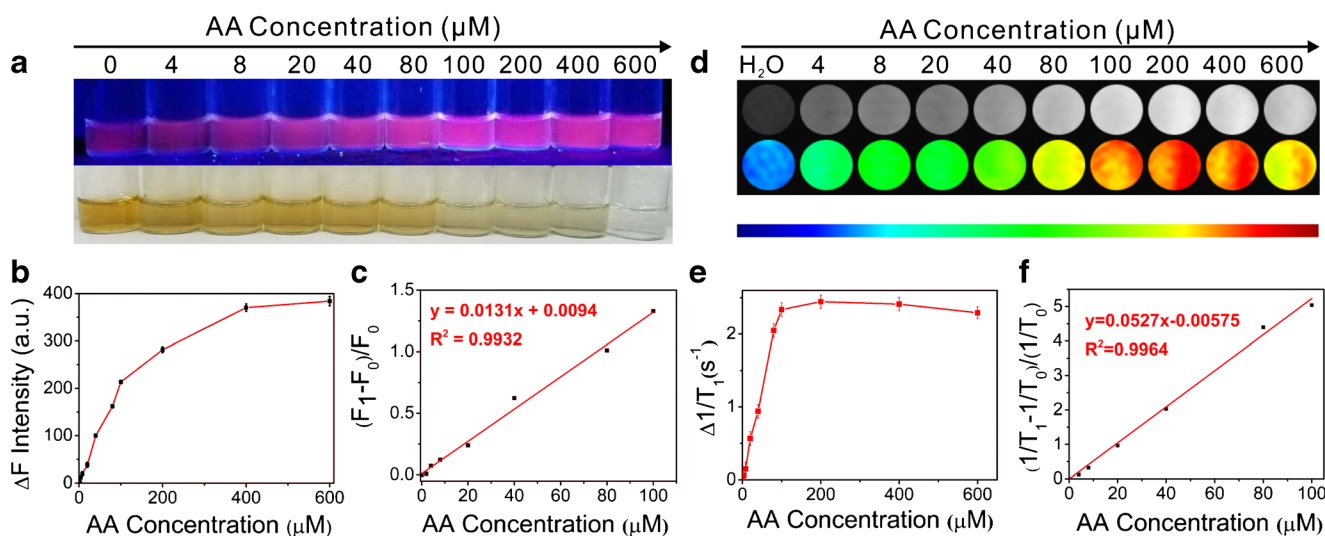

Fig. 3 Studies on sensitivity of blended Au/MnO$_2$@BSA for AA detection in fluorometric/MR modes. **a** Color changes of the blended Au/MnO$_2$@BSA solution under an incandescent lamp and a UV lamp excitation. **b** The growing values of fluorescence intensity. **c** Plotting the value of (F-F$_0$)/F$_0$ against AA concentration over the range from 0 to 100 μM. **d** Under the MR mode, the T$_1$-weighted MR images and false-color-map of the blended Au/MnO$_2$@BSA added with varying AA concentrations (4, 8, 20, 40, 80, 100, 200, 400, and 600 μM) plus water. **e** The growing values of 1/T$_1$. (F) Plotting the value of (1/T$_1$−1/T$_0$)/(1/T$_0$) with AA concentration range from 0 to 100 μM

AA concentration ranging from 0 to 600 μM under a UV lamp excitation. The corresponding fluorescence spectra are exhibited in Fig. S9. The growing values $(F-F_0)$ of fluorescence intensities are plotted in Fig. 3b. And we found a good linear relationship between the values of $(F-F_0)/F_0$ and the concentration of AA ranging from 0 to100 μM, in which F_0 and F are the fluorescence intensities ($\lambda_{ex}/\lambda_{em} = 470/625$ nm) in the absence and in the presence of AA respectively (Fig. 3a). The regression equation is $(F-F_0)/F_0 = 0.0094 + 0.0131C_{AA}$ (C_{AA} is the concentration of AA) with a correlation coefficient of 0.9932. The limit of detection (LOD) for the detection of AA was estimated to be 0.6 μM according to the definition of $LOD = (3\sigma/k)$ where σ is the standard deviation of blank measurements ($n = 10$) and k is the slope of the calibration plot [33]. The detection on the MR mode shows high consistency with that on fluorometric mode. Much similarly, after reaction with AA, the degraded Au/MnO$_2$@BSA shows MR enhancement, and the MR signal intensity is positively relevant to the concentration of the added AA (Fig. 3d). Their relative signal intensities and the growing values of $1/T_1$ are exhibited in Fig. S10 and Fig. 3e. Also, a good linear relationship is obtained at the same AA concentration range (0 to 100 μM) with a correlation coefficient 0.9964 (Fig. 3f). The LOD for the detection of AA was calculated to be 0.4 μM. It is worth noting that when the concentration of AA is greater than 400 μM in the reaction, the growing value experiences a slight downward trend. As we know that the degraded Mn^{2+} ions can be chelated by BSA. This macromolecular binding limits the Mn^{2+} ions rotation, resulting in significant improvement in relaxation rate. However, the extra free AA can compete for Mn^{2+} ions from BSA-Mn^{2+} complex since it also has free carboxyl groups. But we should also know that the resultant AA-Mn^{2+} complex has much lower relaxation rate because the capability of small molecular AA in limiting rotation is much weaker than that of macromolecular BSA [34].

Besides sensitivity, the selectivity of the blended Au/MnO$_2$@BSA is another key property for human serum

detection application. The selectivity study of the blended Au/MnO$_2$@BSA for AA was evaluated by monitoring the both changes of the fluorescence intensity and longitudinal relaxation rate ($1/T_1$). Firstly, the blended Au/MnO$_2$@BSA was incubated with various biologically relevant metal ions, amino acids and redox species, respectively. As shown in Fig. 4a and b, no significant changes are observed in either the fluorometric mode or in MR detection mode, except for Na$_2$S, cysteine, and GSH. Fortunately, the impacts of these three interferents are further effectively inhibited by adding N-ethylmaleimide (NEM) which commonly used as a scavenger, can exclusively react with sulfhydryl compound and eliminates the interference effectively [35]. After adding NEM (0.3 mM), Au/MnO$_2$@BSA is no longer responsive to Na$_2$S, cysteine, and GSH, but its response to AA is not affected.

The above results collectively show that the blended Au/MnO$_2$@BSA have good stability, high sensitivity, in detecting AA under fluorometric and MR mode. Particularly, these two detection modes are highly interacted, providing a cross-validation dual-modal accurate detection.

Cross-validation detection of AA in human serum under fluorometric/MR dual modes

The feasibility of the practical application of the blended Au/MnO$_2$@BSA was demonstrated in the detection of AA in human serum (1/15, v/v) treated by NEM (1.35 μM). By a standard addition method to estimate the concentration of AA in dilute human serum, of which the original concentration of AA in serum was calculated to be 72.343 μM (fluorometric mode) and 89.581 μM (MR mode), respectively. Different concentrations of AA (5, 10, and 15 μM) were spiked respectively into human serum. Finally, the fluorescence and relaxation were measured and compared with the standard AA solution. As shown in the Table 1, under the fluorometric mode, the recoveries of the spiked AA are from 94% to 106%. Under the MR mode, the recoveries are from 107%
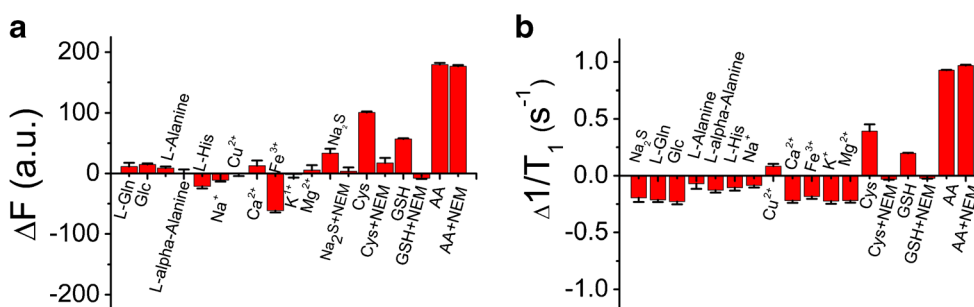

Fig. 4 Selectivity of blended Au/MnO$_2$@BSA for AA detection in fluorometric/MR modes. Under the fluorometric mode (**a**), and the MR mode (**b**), selectivity of the blended Au/MnO$_2$@BSA towards AA or other biological species (Cu^{2+}, Ca^{2+}, Fe^{2+}, Mg^{2+}, K$^+$, Na$^+$, Na$_2$S, L-Gln, Glc, L-alpha-Alanine, L-Alanine, L-His, Cys and GSH). The

concentrations of Cu^{2+}, L-Gln, Glc, L-alpha-Alanine, L-Alanine, L-His, Cys, and GSH were 0.1 mM, while Na$^+$, Ca^{2+}, K$^+$, Mg^{2+}, Fe^{3+} were 1 mM. The N-ethylmaleimide (NEM) concentration was 0.3 mM. Error bars represent the standard deviations of three repetitive experiments

Table 1 Analytical results (mean $\pm$ s; $n = 3$) of the concentrations of AA in human serum sample using our fluorometric/MR dual-mode strategy based on the blended Au/MnO$_2$@BSA

Mode	Found in diluted serum (μM)	Added (μM)	Recovery (%)	R.S.D. (%)
Fluorometric	4.822 ± 0.111	5	106	2.4
		10	103	1.7
		15	94	1.4
MR	5.970 ± 0.107	5	107	1.6
		10	116	1.0
		15	112	1.2

to 116%. These satisfactory recovery values demonstrate the good potential applicability of the blended Au/MnO$_2$@BSA for the quantitative detection of AA in the biological samples. We summarized published fluoroscopic probes for AA detection and made a brief comparison with this work. From Table S1, it is easy to find that for the first time, this work proposes a green one-pot synthesis method that can achieve fluorometric/MR dual-modal cross-validation AA detection at the same time.

Conclusions

In summary, blended Au/MnO$_2$@BSA nanoparticles are synthesized via a one-pot albumin-mediated biomimetic mineralization strategy. This green chemistry can concurrently generate uniform fluorescent Au@BSA and MR-switchable MnO$_2$@BSA nanoparticles. Comparing with other synthetic methods, this approach is environmentally benign and straightforward. The blended Au/MnO$_2$@BSA nanoparticles show AA-induced cross-validation response in fluorometric/MR dual modalities, resulting in fluorometric/MR signal enhancements. Particularly, these dual enhancements are found to be positively correlated with the AA concentration. Based on this principle, the blended Au/MnO2@BSA demonstrates good performance in the detection of AA with high sensitivity and selectivity in a cross-validation fluorometric/MR dual-modal detection fashion. Besides, there are still many challenges for AA imaging due to the interferences from complex components in the cells and living tissues. Thus, the specific responsiveness of nanoprobes to AA still needs to be improved.

References

1. Cheng HJ, Wang XY, Wei H (2015) Ratiometric electrochemical sensor for effective and reliable detection of ascorbic acid in living brains. Anal Chem 87(17):8889–8895
2. Li LB, Wang C, Liu KY, Wang YH, Liu K, Lin YQ (2015) Hexagonal cobalt oxyhydroxide-carbon dots hybridized surface: high sensitive fluorescence turn-on probe for monitoring of ascorbic acid in rat brain following brain ischemia. Anal Chem 87(6):3404–3411
3. Sönmez M, Türk G, Yüce A (2005) The effect of ascorbic acid supplementation on sperm quality, lipid peroxidation and testosterone levels of male Wistar rats. Theriogenology 63:2063–2072
4. Jfy F, Chin SF, Ng SM (2016) A unique "turn-on" fluorescence signalling strategy for highly specific detection of ascorbic acid using carbon dots as sensing probe. Biosens Bioelectron 85:844–853
5. Dong YP, Gao TT, Chu XF, Chen J, Wang CM (2014) Flow injection-chemiluminescence determination of ascorbic acid based on luminol–ferricyanide–gold nanoparticles system. J Lumin 154:350–355
6. Gao X, Yu P, Wang YX, Ohsaka TK, Ye JS, Mao LQ (2013) Microfluidic chip-based online electrochemical detecting system for continuous and simultaneous monitoring of ascorbate and Mg^{2+} in rat brain. Anal Chem 85(15):7599–7605
7. Xiang L, Yu P, Hao J, Zhang M, Zhu L, Dai L, Mao L (2014) Vertically aligned carbon nanotube-sheathed carbon fibers as pristine microelectrodes for selective monitoring of ascorbate in vivo. Anal Chem 86(8):3909–3914
8. Contat-Rodrigo L, Pérez-Fuster C, Lidón-Roger JV, Bonfiglio A, García-Breijo E (2017) Screen-printed organic electrochemical transistors for the detection of ascorbic acid in food. Org Electron 45:89–96
9. Meng HM, Zhang XB, Yang C, Kuai H, Mao GJ, Gong L, Zhang W, Feng S, Chang J (2016) Efficient two-photon fluorescence nanoprobe for turn-on detection and imaging of ascorbic acid in living cells and tissues. Anal Chem 88(11):6057–6063
10. Zhao P, He KY, Han YT, Zhang Z, Yu MZ, Wang HH, Huang Y, Nie Z, Yao SZ (2015) Near-infrared dual-emission quantum dots-gold nanoclusters nanohybrid via co-template synthesis for ratiometric fluorescent detection and bioimaging of ascorbic acid in vitro and in vivo. Anal Chem 87(19):9998–10005
11. Han QX, Dong Z, Tang XL, Wang L, Ju ZH, Liu WS (2016) A ratiometric nanoprobe consisting of up-conversion nanoparticles functionalized with cobalt oxyhydroxide for detecting and imaging ascorbic acid. J Mater Chem B 5:167–172
12. Li N, Li YH, Han YY, Pan W, Zhang TT, Tang B (2014) A highly selective and instantaneous nanoprobe for detection and imaging of ascorbic acid in living cells and in vivo. Anal Chem 86(6):3924–3930
13. Li YX, Chen YT, Huang L, Ma L, Lin Q, Chen GN (2015) A fluorescence sensor based on ovalbumin-modified Au nanoclusters for sensitive detection of ascorbic acid. Anal Methods 7(10):4123–4129
14. Chen YP, Xian Y, Wang Y, Zhang XQ, Cha RT, Sun JS, Jiang XY (2015) One-step detection of pathogens and viruses: combining magnetic relaxation switching and magnetic separation. ACS Nano 9(3):3184–3191

15. Chen X, Xu Y, Li HR, Liu BY (2017) A nanoclay-based magnetic/fluorometric bimodal strategy for ascorbic acid detection. Sensors Actuators B Chem 246:344–351

16. Xu Y, Chen X, Chai R, Xing CF, Li HR, Yin XB (2016) A magnetic/fluorometric bimodal sensor based on a carbon dots-MnO$_2$ platform for glutathione detection. Nanoscale 8(27): 13414–13421

17. Yang WT, Guo WS, Chang J, Zhang BB (2016) Protein/peptide-templated biomimetic synthesis of inorganic nanoparticles for biomedical applications. J Mater Chem B 5(3):401–417

18. Xing XH, Zhang BB, Wang XH, Liu FJ, Shi DL, Cheng YS (2015) An "imaging-biopsy" strategy for colorectal tumor reconfirmation by multipurpose paramagnetic quantum dots. Biomaterials 48:16–25

19. Li D, Hua MH, Fang K, Liang R (2017) BSA directed-synthesis of biocompatible Fe$_3$O$_4$ nanoparticles for dual-modal T$_1$ and T$_2$ MR imaging *in vivo*. Anal Methods 9(21):3099–3104

20. Wang XH, Xing XH, Zhang BB, Liu FJ, Cheng YH, Shi DL (2014) Surface engineered antifouling optomagnetic SPIONs for bimodal targeted imaging of pancreatic cancer cells. Int J Nanomedicine 9: 1601–1615

21. Zhang BB, Jin HT, Li Y, Chen BD, Liu SY, Shi DL (2012) Bioinspired synthesis of gadolinium-based hybrid nanoparticles as MRI blood pool contrast agents with high relaxivity. J Mater Chem 22(29):14494–14501

22. Zhang J, Hao GY, Yao CF, Yu JN, Wang J, Yang WT, Hu CH, Zhang BB (2016) Albumin-mediated biomineralization of paramagnetic NIR Ag$_2$S QDs for tiny tumor bimodal targeted imaging in vivo. ACS Appl Mater Interfaces 8(26):16612–16621

23. Yang WT, Guo WS, Le WJ, Lv GX, Zhang FH, Shi L, Wang XL, Wang J, Wang S, Chang J (2016) Albumin-bioinspired Gd:CuS nanotheranostic agent for in vivo photoacoustic/magnetic resonance imaging-guided tumor-trgeted photothermal therapy. ACS Nano 10(11):10245–10257

24. Xie JP, Zheng YG, Ying JY (2009) Protein-directed synthesis of highly fluorescent gold nanoclusters. J Am Chem Soc 131(3): 888–889

25. Guével XL, Hötzer B, Jung G, Hollemeyer K, Trouillet V, Schneider M (2011) Formation of fluorescent metal (Au, Ag) nanoclusters capped in bovine serum albumin followed by fluorescence and spectroscopy. J Phys Chem C 115(22):10955–10963

26. Wang YL, Cui YY, Gao XY (2012) Bifunctional peptides that precisely biomineralize Au clusters and specifically stain cell nuclei. Chem Commun 48(6):871–873

27. Luo YL (2007) Preparation of MnO$_2$ nanoparticles by directly mixing potassium permanganate and polyelectrolyte aqueous solutions. Mater Lett 61(8):1893–1895

28. Sun SK, Dong LX, Cao Y, Sun HR, Yan XP (2013) Fabrication of multifunctional Gd$_2$O$_3$/au hybrid nanoprobe via a one-step approach for near-infrared fluorescence and magnetic resonance multimodal imaging in vivo. Anal Chem 85(17):8436–8441

29. Zhu WW, Dong ZL, Fu TT, Liu JJ, Chen Q, Li YG, Zhu R, Xu LG, Liu Z (2016) Modulation of hypoxia in solid tumor microenvironment with MnO$_2$ nanoparticles to enhance photodynamic therapy. Adv Funct Mater 26(30):5490–5498

30. Romo-Herrera JM, Alvarez-Puebla RA, Liz-Marzán LM (2011) Controlled assembly of plasmonic colloidal nanoparticle clusters. Nanoscale 3(4):1304–1315

31. Sperling RA, Parak WJ (2010) Surface modification, functionalization and bioconjugation of colloidal inorganic nanoparticles. Philos Trans 47(1):1333–1383

32. Zheng Y, Feng G, Shang T, Wu W, Huang J, Sun D, Wang Y, Li Q (2016) Separation of biosynthesized gold nanoparticles by density gradient centrifugation. Sep Sci 52(2):951–957

33. Huang Y, Zhang Y, Yan ZY, Liao SH (2015) Assay of ceftazidime and cefepime based on fluorescence quenching of carbon quantum dots. Lumin 30(7):1133–1138

34. Zhao ZH, Wang XM, Zhang ZJ, Zhang H, Liu HY, Zhu XL, Li H, Chi XQ, Yin ZY, Gao JH (2015) Real-time monitoring of arsenic trioxide release and delivery by activatable T(1) imaging. ACS Nano 12(2):546–546

35. Cen Y, Tang J, Kong XJ, Wu S, Yuan J, Yu RQ, Chu X (2015) A cobalt oxyhydroxide-modified upconversion nanosystem for sensitive fluorescence sensing of ascorbic acid in human plasma. Nanoscale 7(33):13951–13957